Electronic Supplementary Information:

Atomic Layer Deposition and First Principles Modeling of Glassy Li_3BO_3-Li_2CO_3 Electrolytes for Solid-State Li Metal Batteries

Eric Kazyak,[a] Kuan-Hung Chen,[b] Andrew L. Davis,[a] Seungho Yu,[a] Adrian J. Sanchez,[a] Jose Lasso,[a] Ashley R. Bielinski,[a] Travis Thompson,[a] Jeff Sakamoto,[abc] Donald J. Siegel[abcd] and Neil P. Dasgupta *[a]

[a]*Department of Mechanical Engineering,* [b]*Department of Materials Science and Engineering,* [c]*Michigan Energy Institute, and* [d]*Applied Physics Program, University of Michigan, Ann Arbor, MI 48109, United States*

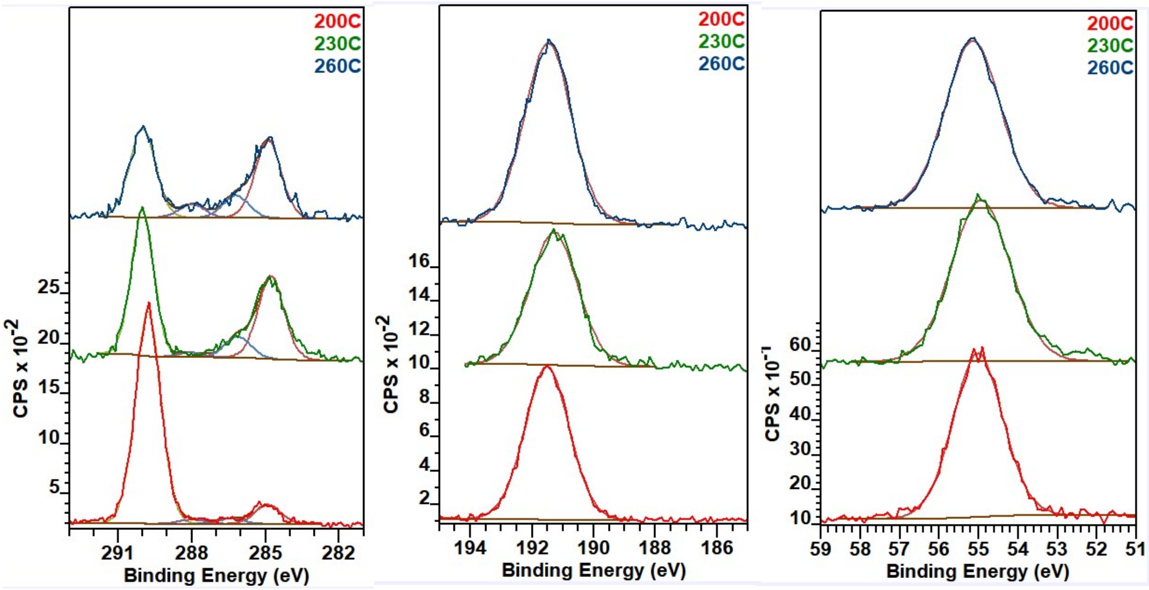

Fig. S1. XPS C 1s Core Scans with components fitted to each carbon containing species. These scans were used to determine the relative amount of Li_2CO_3in the film for deconvolution of the Li_2CO_3 and bridging oxygen in the O 1s core scans shown in Fig. 3.

Due to the proximity of the BO peak to the Li_2CO_3, the C 1s core scans and survey scans were used to further deconvolute the two components. First, the C 1s core scans were fitted with the same 4 components used in our previous work (Supporting Information), and the relative amount of carbon in Li_2CO_3 to total carbon was extracted. Next, assuming a 3:1 ratio of oxygen to carbon as in Li_2CO_3 for charge neutrality and the overall compositions shown in Fig. 3a, the percentage of oxygen associated with Li_2CO_3 can be calculated. This value was then checked against the components fit to the O1s core scans. For all three deposition temperatures, the Li_2CO_3 peak area in the O 1s was within 2% of the value calculated from the C 1s and survey scans. This agreement acts as a check of the peak deconvolution in the O 1s core scans, enabling higher confidence in the following analyses.

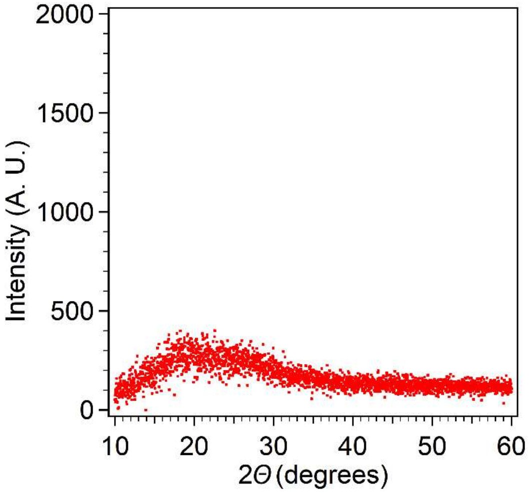

Fig. S2. X-ray diffraction of as-deposited LBCO film at 200°C on glass substrate with no visible diffraction peaks, indicating an amorphous or glassy structure. XRD in was performed using a Rigaku Smartlab X-ray Diffractometer.

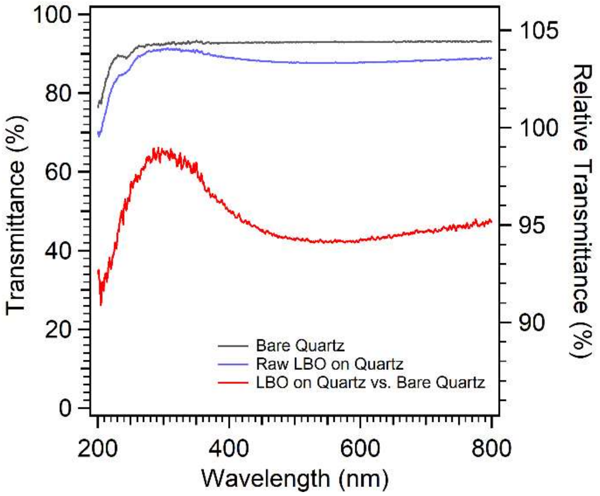

Fig. S3. UV-vis spectroscopy of ~100 nm 200°C as-deposited LBCO ALD film on a quartz substrate. Relative transmittance >90% throughout the measured range is an indication of a large optical bandgap, consistent with the values predicted by DFT calculations.

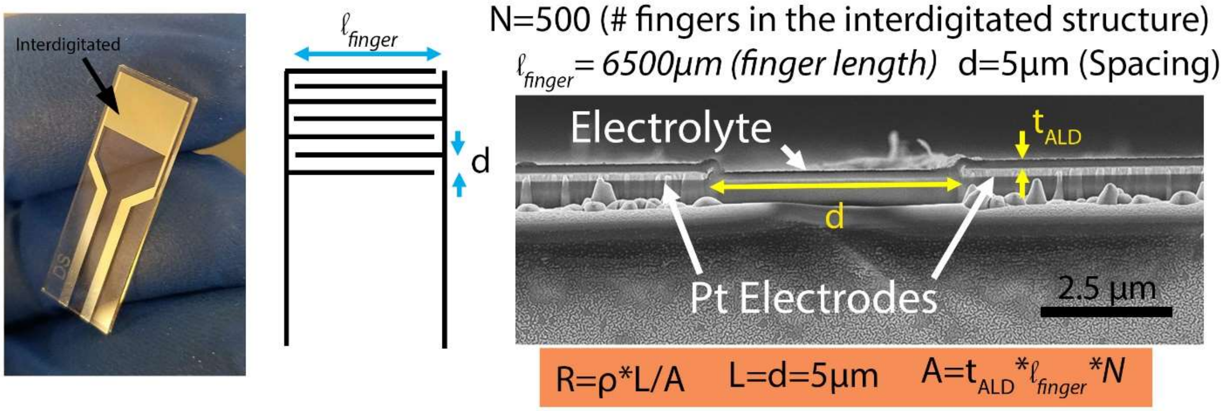

Fig. S4. Schematic and equations detailing how the interdigitated Pt electrodes were used to calculate ionic conductivity in an in-plane cell architecture.

Several through-plane configurations were also used, with electropolished 316 Stainless Steel (TP-Li/SS), Sputtered Gold (TP-Li/Au), and ALD Vanadium oxide on the Stainless Steel (TP-Li/V_2O_5) used as bottom electrodes, and were paired with evaporated Li that was patterned using a shadow mask.

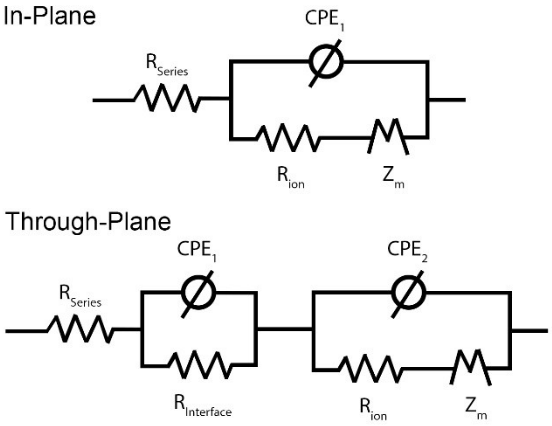

Fig. S5. Equivalent circuit diagrams used to fit ionic conductivity values for the in-plane and through-plane cells.

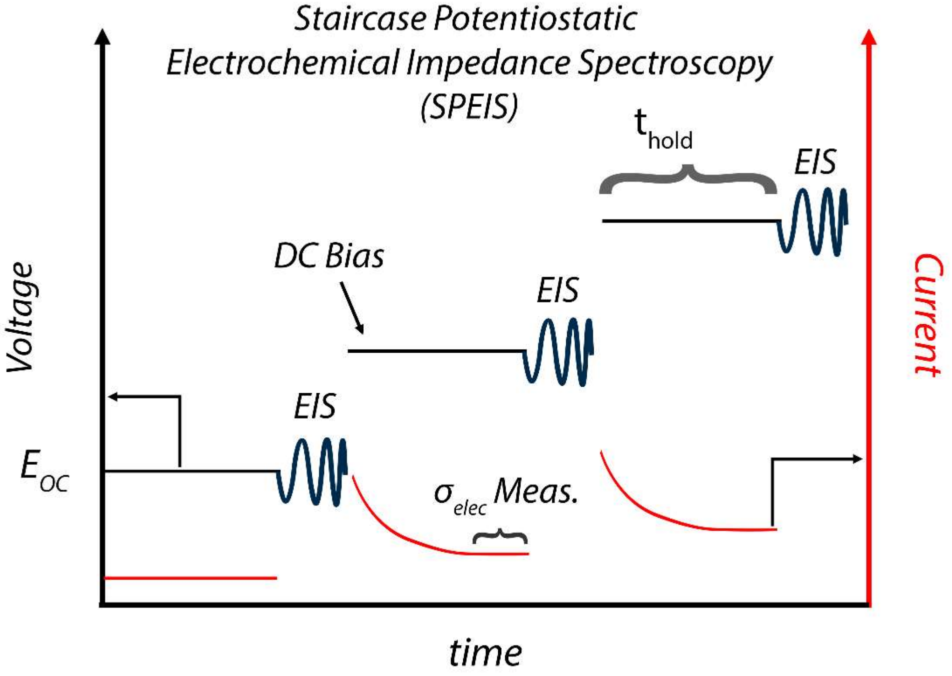

Fig. S6. Schematic description of SPEIS method that was used to measure ionic and electronic conductivities as a function of applied potential in a SS vs. Li blocking/non-blocking cell. A DC bias is applied, after sufficient time for the resulting current to stabilize, an average value is taken in the stable region to determine electronic conductivity. Subsequent EIS is performed about the bias potential to extract ionic conductivity from a fitted Nyquist plot. This procedure continues for a range of applied potentials.

These measurements were again conducted on a Li vs. SS (non-blocking vs. blocking) cell. First, a DC bias is applied to the cell for a certain period of time, in this case 20 minutes. Once the current response has stabilized, an average over the final 100 seconds of the step is taken to determine the electronic conductivity. Then, potentiostatic EIS is done about the DC bias potential, allowing measurement of the ionic conductivity.

Amorphous LBO and LBCO cells were annealed from high temperature using *ab initio* molecular dynamics (AIMD). The quench procedure includes 10 steps ranging from 4500 K to 500 K. AIMD was conducted over 3 ps at 4500 K, 3500 K, 2500 K, and 1500 K, and 5 ps at 1000 K, 900 K, 800 K, 700 K, 600 K, and 500 K. An energy cutoff of 350 eV and Γ-centered 1 × 1 × 1 k-point grid were used for AIMD calculations; the criterion for the electronic self-consistency loop was set to 10^{-4} eV. The NPT ensemble was used to relax the volume and shape of the simulation cells at each target temperature after quench procedure. Subsequently, the NVT ensemble with a Nosé-Hoover thermostat was used for the MSD calculations. The time step of AIMD was 2 fs. Ionic trajectories during AIMD were analyzed to visualize displacements. Iso-surfaces of ionic probability densities are plotted with respect to the mean value of ionic probability density (P_0). Fig. S8 shows iso-surfaces using an iso-value of $2P_0$. Surfaces are plotted for the Li, B, C and O atoms in the LBO and LBCO cells. The probability density isosurfaces for Li are more connected and consume a larger fraction of the cell volume than those in LBO. Fig.s S8 suggest that dynamical contributions from the carbonate anion in LBCO may explain the relatively higher conductivity exhibited by this phase.

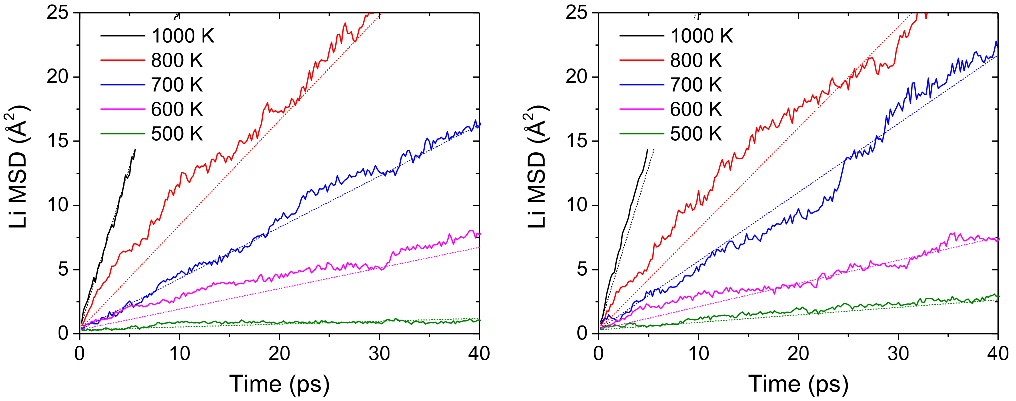

(a) LBO, all temperature (B) LBCO, all temperature

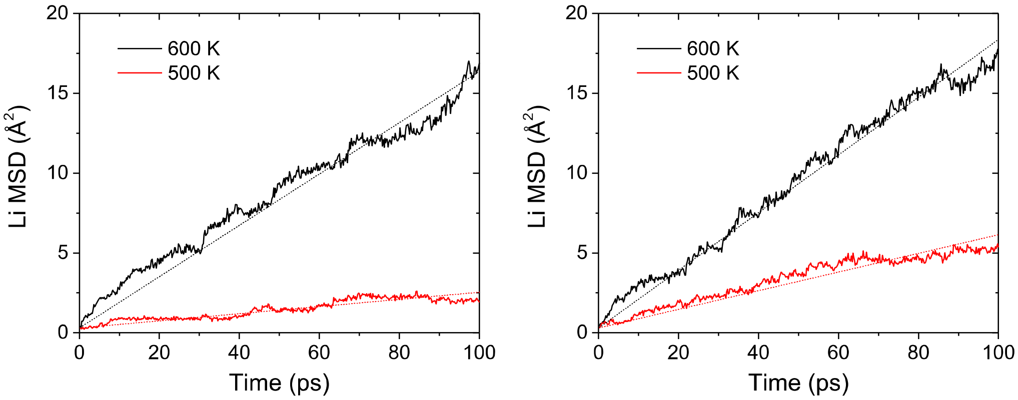

(c) LBO, low temperature (d) LBCO, low temperature

Fig. S7. Calculated mean squared displacement for (a, c) LBO, and (b, d) LBCO. The MSD was evaluated over a 40 ps window for temperatures between 500 and 1000 K, and for a 100 ps window at lower temperatures of 500 and 600 K.

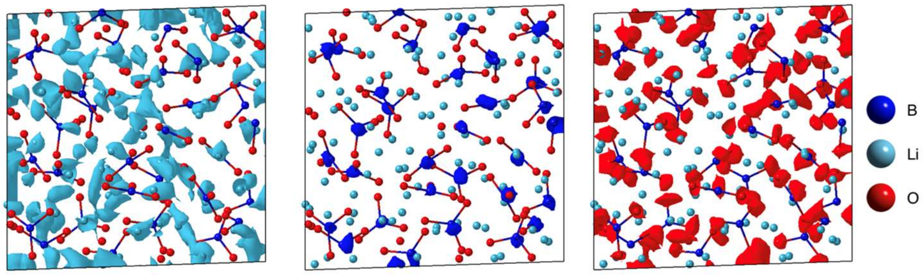

(a) Li in LBO (b) B in LBO (c) O in LBO

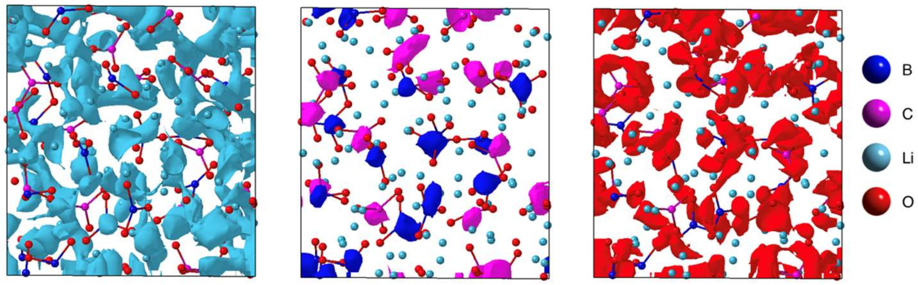

(d) Li in LBCO (e) B and C in LBCO (f) O in LBCO

Fig. S8. Iso-surfaces of the ionic probability density based on ionic trajectories recorded for 60 ps of AIMD at 500 K. The iso-surfaces are plotted using the iso-value equal to $2P_0$. Isosurfaces are plotted for: (a) Li in LBO, (b) B in LBO, (c) O in LBO, (d) Li in LBCO, (e) B and C in LBCO, and (f) O in LBCO.

Table S1. Phase stability for crystalline LBO as function of potential vs Li/Li$^+$.

ϕ (V vs Li/Li$^+$)		Phase equilibria	
0	0.09	Li_2O	LiB
0.09	0.28	Li_2O	$Li_7B_{18}O$
0.28	3.47	Li_3BO_3	
3.47	3.52	O_2	$Li_6B_4O_9$
3.52	3.68	O_2	$LiBO_2$
3.68	3.68	O_2	$Li_2B_4O_7$
3.68	4.21	O_2	$Li_3B_7O_{12}$
4.21	4.43	O_2	$Li_3B_{11}O_{18}$
4.43		O_2	B_2O_3

Table S2. Phase stability of crystalline LCO as function of potential vs Li/Li$^+$.

ϕ (V vs Li/Li$^+$)		Phase equilibria	
0	0.12	Li_2O	LiC_{12}
0.12	1.27	Li_2O	C
1.27	4.10	Li_2CO_3	
4.10		O_2	CO_2

Table S3. Phase stability of amorphous LBCO as function of potential vs Li/Li$^+$.

ϕ (V vs Li/Li$^+$)		Phase equilibria		
0	0.45	Li_2O	LiBC	
0.45	1.27	Li_2O	Li_3BO_3	C
1.27	3.47	Li_3BO_3	Li_2CO_3	
3.47	3.52	O_2	$Li_6B_4O_9$	Li_2CO_3
3.52	3.68	O_2	$LiBO_2$	Li_2CO_3
3.68	4.10	O_2	$Li_3B_7O_{12}$	Li_2CO_3
4.10	4.21	O_2	$Li_3B_7O_{12}$	CO_2
4.21	4.43	O_2	$Li_3B_{11}O_{18}$	CO_2
4.43		O_2	B_2O_3	CO_2

The grand potential phase diagrams[1] for LBO, LCO, and LBCO were obtained using the Pymatgen[2] as function of the Li chemical potential by combining amorphous LBO and LBCO phases from the present DFT calculations with crystalline phases from the Materials Project (MP) database.[3] Amorphous LBO and LBCO are added to the grand potential phase diagrams using the decomposition energy to crystalline phases. The decomposition energy of amorphous LBO to crystalline LBO is 0.072 eV/atom, while amorphous LBCO to crystalline LBO + LCO is 0.071 eV/atom.

Tables S1 through S3 tabulate the phase equilibria for LBO, LCO, and LBCO, respectively, as a function of potential, ϕ, ranging 0-4.5 V (vs. Li/Li^+). Table S1 indicates that crystalline LBO is thermodynamically stable over a relatively wide window, ranging from 0.28 to 3.47 V. The low reduction potential of 0.28 V indicates moderate stability against Li metal. While LBO is not quite as stable as LLZO against Li (0.05 V),[4] it is more stable than other prominent solid electrolytes, such as LiPON (0.68 V) and Li_3PS_4 (1.71 V)[4]. Table S2 summarizes the stability of LCO; its stability window falls within 1.27 to 4.10 V. Thus, it is less stable against Li than LBO, and is reduced to Li_2O and C with the lithiation ($Li_2CO_3 + 4Li \rightarrow 3Li_2O + C$) for potentials below 1.27 V. Finally, Table S3 shows phase stability in the Li-C-B-O quaternary system. Here, amorphous LBCO does not appear as a stable phase for any potential between 0 and 4.43 V.

Table S4. Calculated bandgap for crystalline LBO, amorphous LBO, and amorphous LBCO using the different levels of theory: PBE, HSE06 and the G_0W_0 method. For the latter calculations, two different types of input wavefunctions were used: wavefunctions based on a self-consistent PBE calculation (PBE+G_0W_0), and calculations based on a self-consistent calculation using the HSE06 hybrid functional (HSE06+G_0W_0).

Method	**Crystalline LBO**	**Amorphous LBO**	**Amorphous LBCO**
PBE	5.28	4.51	4.41
HSE06	7.04	6.18	5.98
PBE+G_0W_0	7.73	N/A	N/A
HSE06+G_0W_0	8.52	N/A	N/A

The band gap and density of states (DOS) of LBO and LBCO were predicted using first-principles calculations with a plane wave basis set and the projector augmented wave (PAW) method[5-6], as implemented in the Vienna *Ab initio* Simulation Package (VASP)[7]. Three different levels of theory were used for exchange and correlation contributions: (i) the generalized gradient approximation (GGA) of Perdew, Burke, and Ernzerhof (PBE),[8] (ii) the hybrid functional of Heyd, Scuseria, and Ernzerhof (HSE06),[9-10] and (iii) quasi-particle calculations based on many-body perturbation theory (G_0W_0 method)[11]. The convergence criterion for electronic self-consistency was set to 10^{-5} eV and atoms were relaxed until all forces were smaller than 0.03 eV/Å. An energy cutoff of 600 eV was used for the PBE-based calculations, while a cutoff of 450 eV was used for HSE06 and G_0W_0 calculations. For crystalline LBO, gamma-centered k-point grids with 6 x 6 x 6 and 4 x 4 x 4 densities were used for PBE and HSE06 calculations, and for G_0W_0 calculations, respectively. For amorphous LBO and LBCO, gamma-centered grids with 4 x 4 x 4 and 2 x 2 x 2 densities were used for PBE and HSE calculations, respectively. The calculated structural parameters for crystalline LBO and LCO, and amorphous LBO and LBCO are listed in Table S5. Amorphous models of LBO and LBCO were generated using cubic simulation cell with all atoms randomly positioned. The amorphous LBO cell contained 32 formula units of Li_3BO_3 (total composition of $Li_{96}B_{32}O_{96}$), while the amorphous LBCO cell contained 16 formula units each of Li_3BO_3 and Li_2CO_3 ($Li_{80}B_{16}C_{16}O_{96}$). Amorphous LBO and LCO cells were annealed from high temperature using AIMD. The volume and shape of amorphous cells were relaxed before the DOS calculations.

Based on our HSE06+G_0W_0 calculations, which tends to yield accurate estimates of band gaps,[12] Table S4 shows that crystalline LBO exhibits a large band gap of ~ 8.5 eV. Due to the large size of their simulation cells, GW calculations were not performed on amorphous LBO and LBCO. Nevertheless, at the HSE06 level of theory these amorphous phases exhibit gaps (~6 eV) that are slightly smaller than that of crystalline LBO (~7 eV). Fig. S9 shows the calculated partial DOS for crystalline LBO, amorphous LBO, and amorphous LBCO using the HSE06 functional.

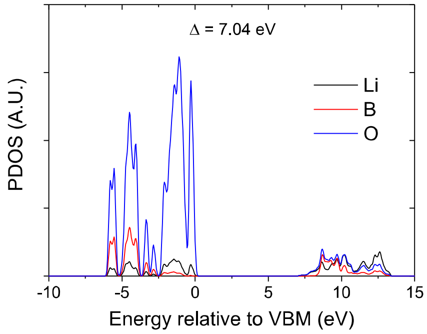

(a) Crystalline LBO

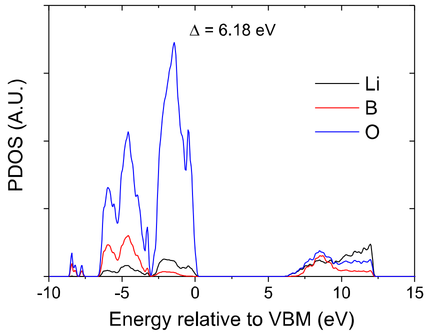

(b) Amorphous LBO

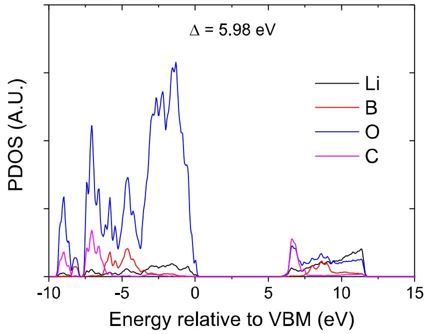

(c) Amorphous LBCO

Fig. S9. Calculated partial density of states for (a) crystalline LBO, (b) amorphous LBO, and (c) amorphous LBCO using the HSE06 hybrid functional. The bandgap for each compound is identified with the symbol Δ. All energies are with respect to the valence band maximum (VBM).

Table S5. Calculated lattice constants for crystalline LBO and LCO, and amorphous LBO and LBCO

Compound	**Composition**	**a (Å)**	**b (Å)**	**c (Å)**	**α (°)**	**β (°)**	**γ (°)**	**Volume (Å^3)**	**Density (g/cm^3)**
Crystalline LBO	4 Li_3BO_3	8.361	9.229	3.290	90	101.2	90	249.10	2.12
Crystalline LCO	4 Li_2CO_3	8.432	5.016	6.312	90	114.7	90	242.62	2.02
Amorphous LBO	32 Li_3BO_3	12.692	12.768	12.586	89.1	88.8	90.0	2039.0	2.08
Amorphous LBCO	$16Li_3BO_3•16Li_2CO_3$	12.421	12.952	12.623	90.1	89.7	92.6	2028.7	2.01

References

(1) Ong, S. P.; Wang, L.; Kang, B.; Ceder, G. Li−Fe−P−O2 Phase Diagram from First Principles Calculations. *Chemistry of Materials* **2008,** *20*, 1798-1807.

(2) Ong, S. P.; Richards, W. D.; Jain, A.; Hautier, G.; Kocher, M.; Cholia, S.; Gunter, D.; Chevrier, V. L.; Persson, K. A.; Ceder, G. Python Materials Genomics (pymatgen): A robust, open-source python library for materials analysis. *Computational Materials Science* **2013,** *68*, 314-319.

(3) Jain, A.; Hautier, G.; Moore, C. J.; Ping Ong, S.; Fischer, C. C.; Mueller, T.; Persson, K. A.; Ceder, G. A high-throughput infrastructure for density functional theory calculations. *Computational Materials Science* **2011,** *50*, 2295-2310.

(4) Zhu, Y.; He, X.; Mo, Y. Origin of Outstanding Stability in the Lithium Solid Electrolyte Materials: Insights from Thermodynamic Analyses Based on First-Principles Calculations. *ACS Appl. Mater. Interfaces* **2015,** *7*, 23685-23693.

(5) Blöchl, P. E. Projector Augmented-Wave Method. *Phys. Rev. B* **1994,** *50*, 17953-17979.

(6) Kresse, G.; Joubert, D. From Ultrasoft Pseudopotentials to the Projector Augmented-Wave Method. *Phys. Rev. B* **1999,** *59*, 1758-1775.

(7) Kresse, G.; Furthmüller, J. Efficient Iterative Schemes for Ab Initio Total-Energy Calculations Using a Plane-Wave Basis Set. *Phys. Rev. B* **1996,** *54*, 11169-11186.

(8) Perdew, J. P.; Burke, K.; Ernzerhof, M. Generalized Gradient Approximation Made Simple. *Phys. Rev. Lett.* **1996,** *77*, 3865-3868.

(9) Heyd, J.; Scuseria, G. E.; Ernzerhof, M. Hybrid Functionals Based on a Screened Coulomb Potential. *J. Chem. Phys.* **2003,** *118*, 8207-8215.

(10) Krukau, A. V.; Vydrov, O. A.; Izmaylov, A. F.; Scuseria, G. E. Influence of the Exchange Screening Parameter on the Performance of Screened Hybrid Functionals. *J. Chem. Phys.* **2006,** *125*, 224106.

(11) Shishkin, M.; Kresse, G. Implementation and Performance of the Frequency-Dependent GW Method within the PAW Framework. *Phys. Rev. B* **2006,** *74*, 035101.

(12) Fuchs, F.; Furthmüller, J.; Bechstedt, F.; Shishkin, M.; Kresse, G. Quasiparticle Band Structure Based on a Generalized Kohn-Sham Scheme. *Phys. Rev. B* **2007,** *76*, 115109.